J Mater Sci: Mater Electron (2026) 37:2416

Enhancing the performance of DSSCs using novel 1,10-Phenanthroline D–π–A sensitizers and Co-doped Eu^{3+}-Ag–TiO_2 photoanodes

Buse Ozsan[1,*], Seyda Aydogdu[1], Arzu Hatipoglu[1], and Ibrahim Erden[1]

[1] *Department of Chemistry, Faculty of Arts and Sciences, Yildiz Technical University, 34220 Istanbul, Turkey*

Received: 10 September 2026
Accepted: 1 November 2026

© The Author(s), under exclusive licence to Springer Science+Business Media, LLC, part of Springer Nature, 2026

ABSTRACT

Dye-sensitized solar cells (DSSCs), as third-generation photovoltaic devices, have attracted considerable attention as alternatives to conventional silicon-based solar cells due to their low cost, simple fabrication, and tunable optical properties. While significant efforts have focused on developing novel organic sensitizers, modifying the titanium dioxide (TiO_2) structure remains a key strategy for enhancing power conversion efficiency (PCE). In this study, novel organic sensitizers (L1 and L2) were strategically designed to increase the PCE of the fabricated devices by directing electron density from the donor group to the 1,10-phenanthroline anchorage via an imidazole bridging unit. Concurrently, the semiconductor material Ag-TiO_2 was co-doped with Eu^{3+} ions to promote rapid and efficient electron transfer at the photoanode interface. The synthesized sensitizers and modified photoanodes were comprehensively characterized using ^{1}H-NMR, MS, UV–Vis spectroscopy, SEM, EDX, and XRF analyses. Density Functional Theory (DFT) and light-harvesting efficiency (LHE) calculations were also performed to provide a fundamental quantum-chemical understanding of the experimental trends. DSSC devices were fabricated using the obtained sensitizers and semiconductor materials, followed by systematic optimization and photovoltaic performance measurements. Among the synthesized sensitizers, L1 exhibited superior photovoltaic performance compared to L2. The highest power conversion efficiency of 0.090% was achieved using the Eu^{3+}-doped Ag–TiO_2 photoanode sensitized with L1, corresponding to a substantial 25% enhancement compared with the undoped L1-based reference device (0.072%). These findings suggest that combining 1,10-phenanthroline-based D–π–A sensitizers, featuring a single phenanthroline anchoring unit with bidentate coordination, with Eu^{3+}-modified Ag–TiO_2 photoanodes may influence the photovoltaic performance of DSSCs.

Address correspondence to E-mail: buse.ozsan@std.yildiz.edu.tr

https://doi.org/10.1007/s10854-026-18850-0
Published online: 10 November 2026

1 Introduction

Among next-generation energy technologies, dye-sensitized solar cells (DSSCs), first introduced in 1991 by O'Regan and Grätzel, have emerged as a highly promising alternative to conventional silicon-based photovoltaic devices [1]. Owing to their low cost, environmental friendliness, and relatively simple fabrication processes, DSSCs are widely regarded as one of the most attractive candidates for sustainable solar energy conversion. Structurally, a typical DSSC architecture consists of a mesoporous semiconductor photoanode, typically a TiO_2 nanoparticle layer deposited on a transparent conducting oxide (TCO) substrate, which is subsequently sensitized with a light-harvesting organic dye molecule. To complete the electrochemical assembly, a platinum-coated counter electrode (CE) serves as the cathode due to its superior electrocatalytic activity and long-term stability, while a liquid electrolyte containing a redox mediator- most commonly the I^-/I_3^- couple- permeates the porous networks of the semiconductor to facilitate efficient charge transport between the electrodes [2].

For efficient operation, sensitizer dyes must exhibit several essential properties. They should strongly absorb light in the visible and near-infrared regions, possess a Lowest Unoccupied Molecular Orbital (LUMO) energy level higher than the conduction band of TiO_2 to enable efficient electron injection, and have a Highest Occupied Molecular Orbital (HOMO) lower than the redox potential of the electrolyte to allow rapid dye regeneration [3]. Over the years, a wide variety of organic and inorganic sensitizers have been investigated to fulfill these criteria. In this context, molecular engineering of sensitizing dyes remains a cornerstone strategy for improving DSSC efficiency. Metal-free organic photosensitizers offer several advantages for dye-sensitized solar cells (DSSCs), including high molar absorption coefficients, structural versatility, relatively straightforward synthesis, and the possibility of tuning their optical and electronic properties through molecular engineering. In particular, the donor–π–acceptor (D–π–A) architecture enables the systematic modification of electron-donating groups, conjugated bridges, and electron-accepting or anchoring units to improve light harvesting and intramolecular charge transfer. However, challenges such as molecular aggregation, inefficient electron injection, and limited long-term photostability may hinder DSSC performance. Therefore, designing sensitizers that combine efficient light absorption, charge injection, and stable surface anchoring is essential for improving device efficiency [4]. The rational design of D–π–A organic photosensitizers is essential for tuning frontier molecular orbital (FMO) energy levels and improving intramolecular charge transfer (ICT), thereby enhancing light harvesting and charge injection in DSSCs [5].

Carbazole-based sensitizers, in particular, have attracted significant interest due to their strong electron-donating capabilities, high stability, and tunable structural frameworks. Koumura et al. demonstrated that the photovoltaic performance of carbazole dyes is largely dependent on the number and position of n-hexyl substituents as well as the thiophene units in the π-bridge, achieving power conversion efficiencies (PCEs) up to 8.3% [6 a–b]. Other research groups have also reported promising results using carbazole donors, such as Tan et al. ($\eta = 6.51\%$), who designed SD7 with triphenylamine as a co-donor, and Yang et al. ($\eta = 4.64\%$), who demonstrated multiple donor systems based on carbazole and rhodanilin derivatives [6c–d]. These findings highlight that carbazole scaffolds continue to be versatile building blocks for generating highly efficient DSSC sensitizers. The variations in photovoltaic responses reported for these carbazole-based sensitizers can be attributed to differences in donor architecture, π-conjugation length, substituent position, and the extent of electronic communication between the donor and acceptor units. Recent computational and experimental explorations on tailored $D-\pi-A$ frameworks emphasize that optimizing the bridging unit and anchoring topology is crucial for minimizing charge recombination and facilitating intramolecular charge transfer (ICT) dynamics across the semiconductor interface [7]. In particular, alkyl substituents can influence the steric environment, molecular packing, solubility, and aggregation behavior of the sensitizer, whereas modification of the π-bridge can alter the degree of intramolecular charge transfer and the absorption profile. Thus, the photovoltaic performance of carbazole-based dyes is determined not only by the electron-donating strength of the carbazole unit but also by its position and its interaction with the π-bridge and anchoring/acceptor groups.

Carboxylic acids, among the various linker groups used to bind sensitizer molecules to TiO_2, are the most commonly utilized due to their strong binding affinities. However, under continuous illumination or

humid conditions, carboxylates can partially detach from the semiconductor surface, thereby reducing dye loading and device stability [8, 9]. Therefore, the development of novel linker groups that provide stronger binding, improved charge injection, and enhanced photostability remains a critical research direction. In this context, 1,10-phenanthroline derivatives have attracted attention due to their rigid planar structures, electron acceptor capabilities, and capacity to act as multidentate chelating units. Furthermore, they can serve simultaneously as a linker group and an electron acceptor in donor-π-acceptor (D–π–A) type sensitizers. Employing a single phenanthroline anchoring unit capable of bidentate coordination not only reinforces the dye-chemisorption stability on the TiO_2 surface compared to conventional monodentate carboxylate linkers, but also provides a well-defined electronic pathway for efficient electron injection into the conduction band [7]. In this context, the integration of specific functional anchoring motifs capable of bidentate chelation plays a crucial role in securing robust dye adsorption onto the semiconductor photoanode, thereby facilitating efficient interfacial electron transfer and enhancing the overall stability and performance of dye-sensitized solar cells [10]. Unlike conventional monodentate anchoring groups (such as carboxylic or cyanoacrylic acids) that often suffer from partial desorption under prolonged illumination or humid environments, the 1,10-phenanthroline anchoring unit provides a robust, rigid planar platform capable of bidentate chelation onto the mesoporous TiO_2 surface through its two rigid nitrogen heteroatoms. Unlike conventional monodentate anchoring groups, 1,10-phenanthroline offers a rigid, planar structure that can coordinate to the TiO_2 surface through its two nitrogen atoms, potentially improving adsorption stability and surface coverage. Furthermore, its electron-deficient conjugated framework can facilitate electronic coupling between the excited dye and TiO_2, supporting electron injection and influencing interfacial charge recombination [11–13].

Although 1,10-phenanthroline is widely used in coordination chemistry and metal complex photosensitizers, its application as an organic linker group in DSSCs remains scarce. Only a few studies in the literature report the use of 1,10-phenanthroline as an anchoring unit in DSSCs. Zhang et al. (2015) synthesized two donor–acceptor type organic dyes containing 1,10-phenanthroline as a linker group. These dyes were efficiently adsorbed onto TiO_2 surfaces and achieved a maximum PCE of 4.04%, demonstrating that 1,10-phenanthroline can serve as both an electron acceptor and a linker unit [14]. Similarly, Jia et al. (2019) designed two metal-free organic sensitizers (S1 and S2) with a 2D–π–2 A framework using 1,10-phenanthroline as a linker group. The resulting DSSCs showed improved electron injection efficiency and dye adsorption stability, achieving a PCE of 4.39% for S1 [15]. In addition, we recently reported two metal-free organic dyes (B1 and B3) with a D–π–A architecture containing triphenylamine as an electron donor, an imidazole π-bridge, and 1,10-phenanthroline as the anchoring unit. That study showed that the multiple linker design in B3 enhanced charge localization and electron injection efficiency, improving DSSC performance by approximately twofold compared to the single-linker B1 system [16].

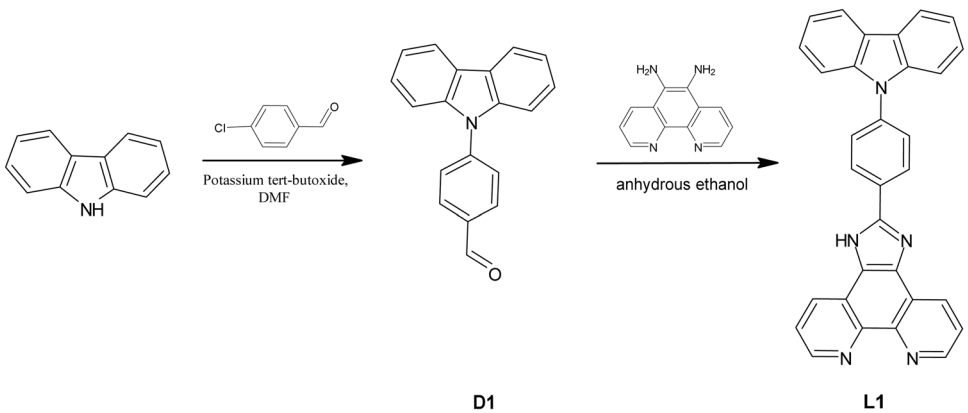
While optimizing the organic sensitizer is crucial, customization of the semiconductor photoanode through elemental doping has also emerged as a powerful parallel strategy to enhance DSSC performance. Specifically, modification of TiO_2 with precious metal nanoparticles such as Ag, Au, and Pt, or the addition of rare-earth ions including Eu^{3+}, Tb^{3+}, Gd^{3+}, and Sm^{3+}, has been shown to improve light harvesting and suppress charge recombination. Ag nanoparticles generate localized surface plasmon resonance (LSPR), which significantly increases visible light absorption and facilitates faster electron injection [17]. Meanwhile, rare-earth ions, particularly Eu^{3+}, can modulate charge recombination pathways while promoting electron transport by creating additional energy states within the band structure. The combined effects of doping have been reported to improve charge separation and photovoltaic performance, with power conversion efficiencies ranging from 5 to 8% [18, 19]. The strategic co-doping of TiO_2 with noble metal plasmonic nanoparticles and rare-earth ions establishes a dual-function photoanode platform that simultaneously broadens visible-light harvesting via Localized Surface Plasmon Resonance (LSPR) and suppresses charge recombination through engineered intra-band trap states [7].

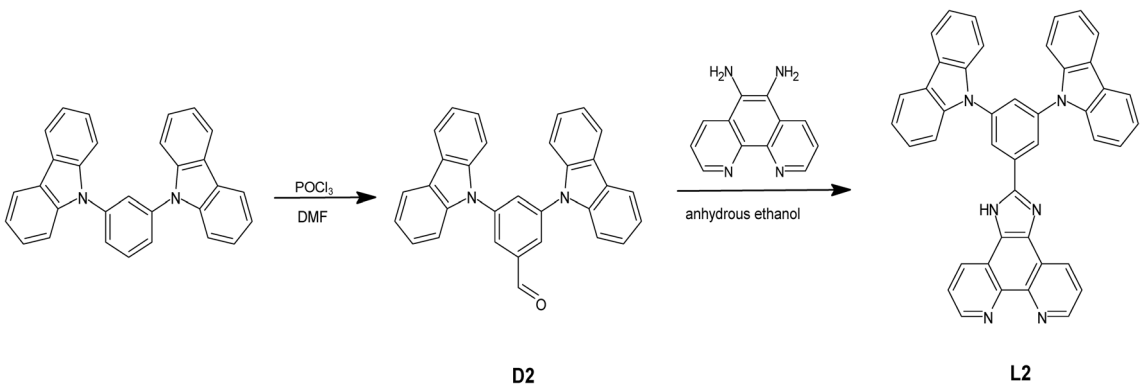
The aforementioned literature reports demonstrate the photovoltaic potential of phenanthroline-containing sensitizers under their respective optimized device conditions; however, disparities in sensitizer architecture, semiconductor morphology, electrolyte composition, and fabrication procedures render direct numerical comparisons with the present study inappropriate.

Despite these individual advances in dye and anode engineering, two major gaps remain in the literature: (i) few studies have explored phenanthroline-based D–π–A organic dyes featuring a single phenanthroline anchor with bidentate coordination, and (ii) the integration of such dyes with rare-earth and silver co-doped TiO_2 photoanodes has not yet been systematically investigated. The present work therefore focuses on evaluating the material compatibility and photovoltaic response of a phenanthroline-based D–π–A sensitizer featuring a single phenanthroline anchor with bidentate coordination, assembled with a Eu^{3+}-modified Ag–TiO_2 photoanode. Combining engineered organic sensitizers with tailored Ag–TiO_2-RE (rare-earth) semiconductors is expected to yield significant benefits through enhanced light harvesting, increased electron injection efficiency, and suppressed charge recombination.

In this study, two novel metal-free organic sensitizers, designated as L1 and L2, featuring a well-tailored donor–π–acceptor (D–π–A) architecture were strategically designed and successfully synthesized (Schemes 1 and 2). Within these molecular frameworks, electron-donating carbazole derivatives were coupled via an imidazole bridging unit to a 1,10-phenanthroline moiety, creating a robust anchoring platform capable of bidentate coordination on the semiconductor surface. To gain deeper insights into their underlying electronic structures, the frontier molecular orbital layouts, energy levels, and intramolecular charge transfer (ICT) dynamics of L1 and L2 were systematically investigated through comprehensive Density Functional Theory (DFT) calculations. Concurrently, to mitigate the intrinsic charge recombination limitations of conventional photovoltaics, engineered Eu^{3+}-doped Ag–TiO_2 nanostructures were developed and employed as advanced semiconductor photoanodes, explicitly tailored to accelerate interfacial electron transport kinetics and extend light-harvesting capabilities in the visible region. The overall photovoltaic performances of the fabricated DSSCs were rigorously evaluated under simulated AM 1.5 G solar illumination (100 mW cm^{-2}). Ultimately, this systematic optimization highlights the potential of combining

Scheme 1 Synthesis route of compound L1 used as a sensitizer





Scheme 2 Synthesis route of compound L2 used as a sensitizer

1,10-phenanthroline-based D–π–A sensitizers featuring a single phenanthroline anchor with bidentate coordination with europium-modified Ag–TiO_2 photoanodes, providing insights into the development of efficient dye-sensitized solar cells with improved photovoltaic performance.

2 Experimental

2.1 Materials and characterization

All chemicals and solvents used in this study were of analytical grade and sourced from commercial suppliers. The FTIR spectra were obtained using a Spectrum One Perkin Elmer 1600 FTIR spectrophotometer. ^{1}H NMR spectra were recorded on a Varian UNITY INOVA 500 MHz NMR spectrometer with $CDCl_3$ and MeOH as the solvent. Absorption spectra were measured using a Shimadzu-2600 UV–Vis spectrophotometer. Q-TOF mass spectra were measured on Agilent Technologies, 6530.

2.2 Device preparation

The preparation of DSSC devices was carried out as follows: Fluorine doped tin oxide (FTO) substrates were purchased from Spi Co. Ltd. The substrates were cleaned using an ultrasonic bath with a solution of acetone and isopropanol, followed by rinsing with distilled water for 10 min. They were dried with nitrogen gas to ensure optimal mechanical contact between the conductive FTO surface and titanium dioxide (TiO_2), as well as to protect the FTO surface from interaction with the electrolyte. The photoanodes consist of 15–20 μm thickness TiO_2 and Ag/Eu-modified TiO_2 were prepared following the procedure reported in the literature [20], with modifications where applicable. For the modified photoanodes, The synthesized Ag/Eu-modified TiO_2 powder was dispersed in ethanol in the presence of a few drops of acetic acid to obtain a homogeneous suspension. The resulting suspension was deposited onto the cleaned FTO substrates using the doctor-blade technique. The coated films were subsequently heated in air at 400 °C for 3 h.

After the sintering step, the photoanodes were cooled to room temperature and immersed in separate dye solutions containing L1 or L2 at a concentration of 1×10^{-4} M at room temperature for 24 h. Finally, the dye-sensitized photoanodes were assembled with platinized FTO counter electrodes by manually pressing the electrodes together to fabricate the DSSC devices. The platinized FTO glass was made by exposing it to H_2PtCl_4 solution followed by heating at 450 °C for 10 min.

After drying under an air stream, the sensitized Titania electrode was sandwiched with a thermally platinized counter electrode separated and sealed. The electrolyte solution, composed of 0.5 M potassium iodide and 0.05 M iodine dissolved in pure ethylene glycol, was prepared following the procedure outlined by Smestad [21]. The electrolyte was injected into the gap between the electrodes by capillarity. The active area of the devices, determined by the overlapping regions of the anode and cathode, was set to 1 cm^2. The photovoltaic performance is determined under simulated sunlight. The current density versus voltage (J-V) characteristic of the cells were measured both in the dark and under simulated ABET 1.5 G solar illumination by using a Keithley 2400 Digital Source Meter at room temperature.

2.3 Synthesis

5-Nitro-1,10-phenanthroline [22], 5-Nitro-6-amino-1,10-phenanthroline [23], 5,6-Diamino-1,10-phenanthroline [23] were synthesized according to the literature.

2.3.1 *Synthesis of the D1 donor group*

Carbazole (8.4 g, 0.05 mol) was dissolved in 200 mL of N,N-dimethylformamide (DMF). Potassium tert-butoxide (5.5 g, 0.05 mol) was added to the solution and the mixture was stirred for 30 min. Then, a solution of 4-chlorobenzaldehyde (0.06 mol) was added dropwise, and the reaction mixture was stirred at the same temperature under reflux for 36 h. After the reaction was complete, the mixture was poured into ice water, and the resulting precipitate was separated by filtration. The crude product was purified by recrystallization from a 10:1 (v/v) acetone/water mixture, yielding pale yellow crystals (Scheme 1).

2.3.2 *Synthesis of the D2 donor group*

Phosphorus oxychloride ($POCl_3$, 4 mL, 52 mmol) was slowly added dropwise to 30 mL of DMF at room temperature, stirring constantly. Approximately 1 h later,

1,3-bis(N-carbazolyl)benzene (0.82 g) was added to the mixture. The reaction was stirred under reflux at 100 °C for 6 h in a nitrogen atmosphere. After cooling to room temperature, the reaction mixture was poured into 100 mL of ice water, and the resulting precipitate was filtered under vacuum. The crude product was monitored by TLC and purified by column chromatography (n-hexane/dichloromethane, 2:1). The resulting yellow pure product was dried under vacuum (Scheme 2).

2.3.3 Synthesis of compound L1

5,6-Diamino-1,10-phenanthroline (0.03 g, 0.142 mmol) was dissolved in 30 mL of anhydrous ethanol and added dropwise to 4-carbazol-9-yl-benzaldehyde (0.0385 g, 0.142 mmol) dissolved in 10 mL of anhydrous ethanol. The reaction mixture was stirred at 90 °C for 12 h under argon gas. The solvent was evaporated by rotary evaporator until one third of the initial volume remained, and petroleum ether was added at room temperature. When the solution was cooled to room temperature, a yellow precipitate was obtained. The resulting precipitate was filtered and then recrystallized from 2:1 n-hexane/ethyl acetate. FTIR (KBr, cm^{-1}): 3450 (N–H), 3048 (aromatic C–H), 1602 (C = N), 1450 (C = C), 1325 (C–N), 1235 (C–N), 990 (C–H). ^{1}H NMR (500 MHz, MeOH, δ ppm): 8.87 (d, 2 H), 8.82 (d, 2 H), 8.70 (d, 2 H), 8.50 (d, 2 H), 8.24 (s, 1 H), 7.90 (d, 2 H), 7.63 (m, 2 H), 7.30 (d, 2 H), 7.23 (t, 2 H), 7.01 (t, 2 H). MS (ESI): m/z $[M+1]^+ = 462.17$ ($C_{31}H_{19}N_5$, M.W. 461.5 g/mol) [24].

2.3.4 Synthesis of compound L2

5,6-Diamino-1,10-phenanthroline (0.03 g, 0.142 mmol) was dissolved in 30 mL of anhydrous ethanol and added dropwise to compound D2 (0.062 g, 0.142 mmol) dissolved in 10 mL of anhydrous ethanol. The reaction mixture was stirred under argon gas at 90 °C for 12 h. The solvent was evaporated by rotary evaporator until one-third of the initial volume remained, and petroleum ether was added at room temperature. When the solution was cooled to room temperature, a yellow precipitate was obtained. The resulting precipitate was filtered and then recrystallized from 2:1 n-hexane/ethyl acetate. FTIR (KBr, cm^{-1}): 3367 (N–H), 3060 (aromatic C–H), 1596 (C = N), 1447 (C = C), 1250 (C–N), 1020 (C–H). ^{1}H NMR (500 MHz, MeOH, δ ppm): 7.15 (m, 4 H), 7.31 (m, 4 H), 7.37 (d, 4 H), 7.65 (dt, 1 H), 7.69 (dt, 1 H), 8.01 (d, 2 H), 8.16 (s, 1 H), 8.27 (s, 1 H), 8.58 (d, 4 H), 8.64 (d, 1 H), 8.69 (d, 1 H), 8.86 (d, 1 H), 8.90 (d, 1 H). MS (ESI): m/z $[M+1]^+ = 627.23$ ($C_{43}H_{26}N_6$, M.W. 626.23 g/mol).

2.4 Modification of TiO_2 photoanodes

For the preparation of the modified TiO_2 photoanodes, 1 mL of titanium tetraisopropoxide (TTIP) was added to 50 mL of ethylene glycol in a beaker, and the mixture was continuously stirred for 10 h at room temperature. Subsequently, 100 mL of acetone and 1 mL of deionized water were introduced into the solution, followed by further stirring for 2 h to induce the formation of a homogeneous suspension. To this suspension, 100 mg of silver nitrate ($AgNO_3$) and 50 mg of europium(III) nitrate hexahydrate [$Eu(NO_3)_3 \cdot 6H_2O$] were sequentially added, and the mixture was stirred for an additional 10 h. The resulting precipitate was isolated via centrifugation, washed thoroughly with deionized water and absolute ethanol to remove residual impurities, and subsequently dried at 100 °C for 10 h.

2.5 Computational method

The geometrical structures of the compounds for ground state were optimized by using DFT with B3LYP/6-31 g(d) level in Gaussian 09 programme [25]. The verification of the geometries as global minimum was done with frequency calculations with no imaginary frequencies. The absorption spectrums of the compounds were calculated in methanol by using Time Dependent Density Functional Theory (TD-DFT), in associated with Conductor- Like Polarizable Continuum Model (PCM) [26, 27]. The anharmonic corrections for vibrational frequencies were done by multiplying values with 0.983 for below 1700 cm^{-1}, and 0.958 for above 1700 cm^{-1}, respectively [28]. The same level of the theory was adopted for obtaining ^{1}H NMR of compound by using Gauge Independent Atomic Orbital (GIAO) approach [29].

To investigate the electronic structure of compounds, the Molecular Electrostatic Potential (MEP) surface and Boundary Molecular Orbitals (FMO) were calculated. Additionally, the reactive nature of the compounds was discussed with the calculated global reactivity parameters. Using Koopman's Theorem chemical potential (μ), hardness (η), electrophilic

index (ω), and softness (S) were calculated. According to this theory ionization potential (I), and electron affinity (A) of the compounds are related to negative energy values of the Lowest Unoccupied Orbital (LUMO), and Highest Occupied Orbital (HOMO), respectively [30]. The formulas for global reactivity parameters are given below with Eq. 1–4.

$$\mu = \frac{1}{2}\left(\frac{\partial E}{\partial N}\right)_{V(r)} \approx \frac{(I+A)}{2} \approx \frac{E_{LUMO}+E_{HOMO}}{2} \quad (1)$$

$$\eta = \frac{1}{2}\left(\frac{\partial^2_E}{\partial N^2}\right)_{V(r)} \approx \frac{(I-A)}{2} \approx \frac{E_{LUMO}-E_{HOMO}}{2} \quad (2)$$

$$\omega = \frac{\mu^2}{2\times\eta} \quad (3)$$

$$s = \frac{1}{2\times\eta} \quad (4)$$

In which N, $V_{(r),}$ and E are the number of electrons, potential,and the total energy, respectively. [30–32]. The calculated visualizations of compounds were prepared with GaussView 05 package programme [33].

3 Results and discussion

3.1 Characterization

Sensitizers represent the most critical components in achieving high power conversion efficiency (PCE) in dye-sensitized solar cells (DSSCs). The key parameters governing DSSC performance include the efficient light absorption of the sensitizer molecules, the facilitation of electron–hole separation, and robust binding to the TiO_2 surface to enable efficient electron injection. Within the scope of this study, metal-free organic sensitizers L1 and L2 were designed incorporating a 1,10-phenanthroline anchor group, which provides a high adsorption capacity onto the TiO_2 surface via the two nitrogen heteroatoms within its framework. The photovoltaic performances of the fabricated DSSCs were systematically evaluated utilizing the synthesized dyes as sensitizers on the Eu^{3+}-doped Ag-TiO_2 photoanodes.

The L1 and L2 dyes feature a D–π–A type architecture tailored to promote an intramolecular charge transfer (ICT) mechanism. In this configuration, electron-donating carbazole derivatives direct the electron density from the donor moiety to the single 1,10-phenanthroline anchor through an imidazole bridging unit. This molecular design aligns with the single phenanthroline anchor approach, which is well-documented in the literature for its pronounced intramolecular charge-transfer capacity and the bidentate coordination ability of the phenanthroline unit, facilitating its interaction with the semiconductor TiO_2 surface. The synthesis of the designed dyes was executed via the formation of the imidazole ring, reacting the aldehydes (D1 and D2) derived from the carbazole derivatives with 5,6-diamino-1,10-phenanthroline. The synthesized sensitizers were structurally and optically characterized using FTIR, UV–Vis spectroscopy, ^{1}H NMR spectroscopy, and mass spectrometry. The resulting spectroscopic and mass-spectrometric data provide complementary and definitive evidence supporting the proposed molecular structures.

The experimental UV–Vis absorption spectra of the synthesized L1 and L2 compounds (Figure SI.2 and Figure SI.3) exhibited characteristic π–π^* transitions in the 250–350 nm range and n–π^* transitions within the 350–400 nm region, as theoretically anticipated. In dye-sensitized solar cell (DSSC) applications, extending the light-harvesting capability of sensitizers toward longer wavelengths is vital for achieving enhanced power conversion efficiency (PCE). To further elucidate the optical properties, the calculated UV–Vis spectral data for both compounds are summarized in Table 1.

Table 1 Simulated UV–Vis Absorption Properties and Corresponding Electronic Transitions of L1 and L2 Dyes

	Transition	Contribution (%)	$\lambda(nm)$	$E_{ex}(eV)$	f
L1	HOMO → LUMO	91.29%	370.19	3.35	0.7515
	HOMO → LUMO + 1	6.23%			
L2	HOMO-2 → LUMO	56.85%	343.23	3.61	0.3427
	HOMO-2 → LUMO + 1	19.55%			
	HOMO-1 → LUMO + 1	7.23%			
	HOMO → LUMO + 1	8.69%			

The primary electronic transition for the L1 compound was found to originate from the HOMO to the LUMO orbital (91.29%), featuring an excitation energy (E_{ex}) of 3.35 eV and an oscillator strength (f) of 0.7515. Furthermore, the calculated maximum absorption wavelengths (λ_{max}) were determined as 370.19 nm and 343.23 nm for L1 and L2, respectively (Table 1). The relative errors between the experimental and theoretical maximum absorption wavelengths were calculated as 4.54% for L1 and 13.14% for L2, demonstrating an acceptable agreement with the computational model. This verifies the suitability of the computational model. Since the experimentally obtained results are affected from the experimental conditions, such a difference between experimental and calculated results are acceptable [34].

The experimental and calculated FTIR spectra of compounds L1 and L2 (Figure SI.5 and Figure SI.6) were analysed to confirm their structural frameworks. In accordance with the literature, the experimental (calculated) spectra exhibited characteristic vibrational bands corresponding to the N–H stretching at 3450 (3509.70) cm^{-1} and 3367 (3504.60) cm^{-1}, C = N stretching at 1602 (1636.86) cm^{-1} and 1596 (1543.48) cm^{-1}, C = C aromatic stretching at 1450 (1423.85) cm^{-1} and 1447 (1486.93) cm^{-1}, and C–N stretching at 1325 (1332.96) cm^{-1} and 1250 (1511.27) cm^{-1}. A comprehensive comparison between the experimentally obtained frequencies and the theoretically calculated values is summarized in Table SI-1. Crucially, the characteristic primary amine $(-NH_2)$ stretching doublet of the 5,6-diamino-1,10-phenanthroline precursor (typically observed at 3370 and 3267 cm^{-1}) is no longer observed as such, and the sharp $C = O$ stretching band located at 1695 cm^{-1} in the starting aldehydes (D1 and D2) completely disappears in the FTIR spectra of the final L1 and L2 molecules. Concurrently, the appearance of a single N–H stretching band at 3450 cm^{-1} for L1 and 3367 cm^{-1} for L2 confirms the successful cyclization and formation of the imidazole ring.

The successful formation of the target architectures was unequivocally validated by monitoring the diagnostic changes in the ^{1}H-NMR spectra (Figure SI.8 and Figure SI.9). The broad proton signal corresponding to the $–NH_2$ group, originally observed at 4.4 ppm in the 5,6-diamino-1,10-phenanthroline precursor, completely disappears in the spectra of the final products. Concurrently, a sharp singlet assigned to the N–H proton of the newly formed imidazole ring emerges at experimental (calculated) chemical shifts of 8.24 (8.44) ppm for L1 and 8.27 (8.46) ppm for L2. This significant spectral evolution confirms the successful cyclization and formation of the imidazole ring. Furthermore, the characteristic aldehyde proton signals, typically observed at approximately 9.5 ppm in the precursor compounds D1 and D2 (obtained via the formylation of the carbazole moiety), are entirely absent in the NMR profiles of L1 and L2. The complete disappearance of the aldehyde proton signal provides complementary verification of the target architectures. Overall, the experimentally obtained chemical shifts correlate well with the theoretically calculated NMR datasets (Table SI.2).

The molecular weights of the synthesized sensitizers were precisely confirmed via Q-TOF mass spectrometry. In the HRMS spectrum of compound L1 (Figure SI.10), the characteristic molecular ion peak was observed at m/z: 462.16, while the spectrum of compound L2 (Figure SI.11) exhibited the corresponding molecular ion peak at m/z: 627.23. Taken together, the comprehensive analysis of all obtained spectroscopic and spectrometric datasets unequivocally confirms the successful synthesis and structural integrity of the proposed molecular architectures.

The surface morphology and elemental composition of the synthesized Eu^{3+}-doped Ag-TiO_2 photoanode film were comprehensively evaluated via FE-SEM micrographs at sequential magnifications and EDX spectroscopy, as illustrated in (Fig. 1). The FE-SEM analysis at increasing magnifications establishes a well-defined correlation from the macro-scale topography down to the primary nanoscale features. The low-magnification micrograph at 50,000 × (Fig. 1d) confirms the formation of a continuous, crack-free, and homogeneous surface with high macroscopic roughness, which is highly advantageous for securing reliable electronic transport paths. As the magnification increases to 100,000 × and 200,000 × (Fig. 1c and b), the interconnected mesoporous junctions and uniform distribution of nanoparticle aggregates become distinctly visible. These continuous porous networks serve as crucial ion-diffusion pathways, facilitating efficient infiltration of the liquid redox electrolyte within the DSSC assembly. At the highest resolution of 400,000 × (Fig. 1a), direct scale measurements reveal that the primary nanoparticles exhibit a spherical morphology with an average diameter of ~ 9.59 nm, thereby ensuring a highly expanded specific surface area required for maximized dye chemisorption.

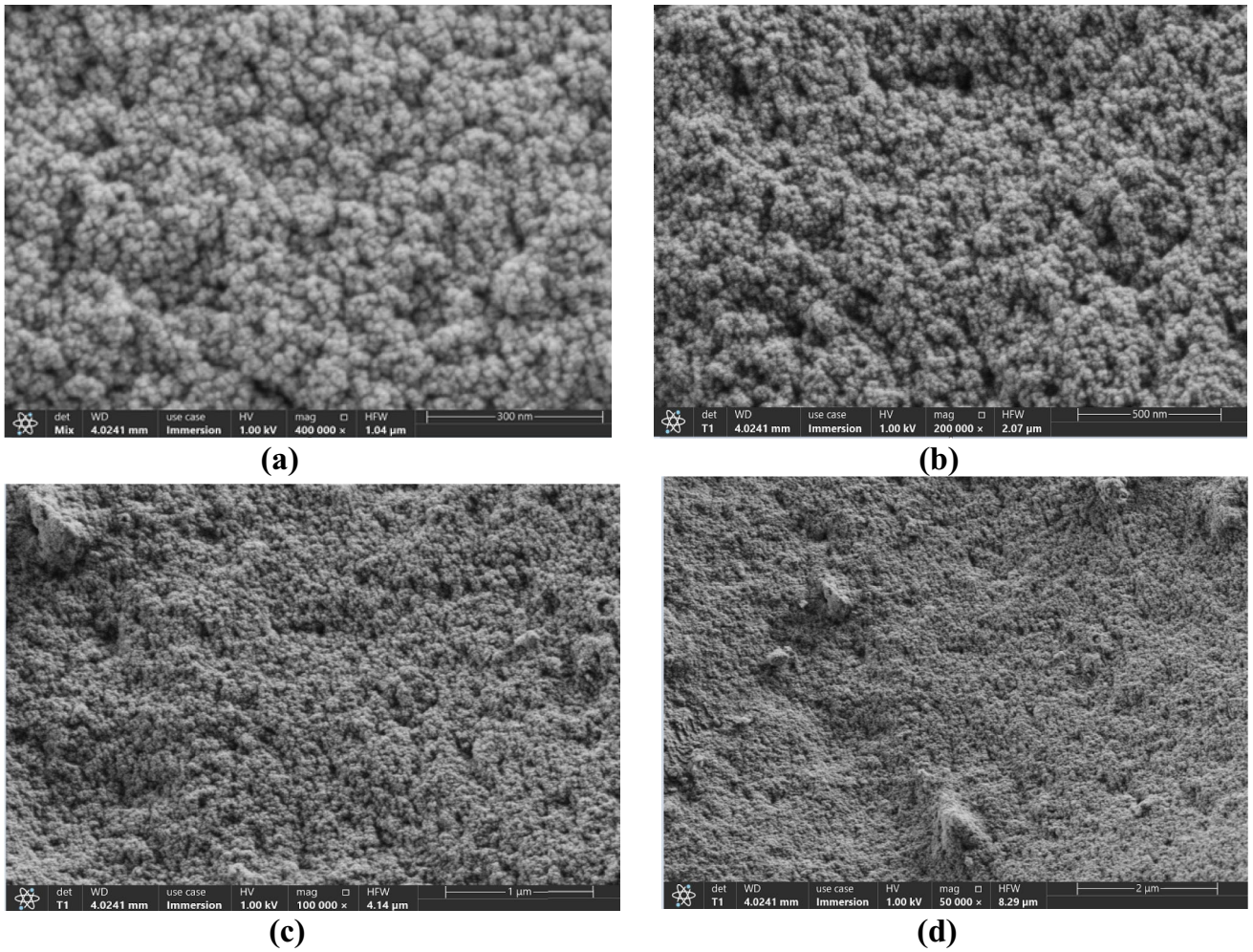


Fig. 1 FE-SEM images of Ag/TiO_2:Eu co-doped film at different magnifications: **a** 400,000 × showing primary nanoparticles (~ 9.59 nm), **b** 200,000 × high lighting mesoporous junctions, **c** 100,000 × showing uniform aggregates, and **d** 50,000 × demonstrating continuous, crack-free surface topography

The structural integrity and chemical composition of the nanostructured photoanode were validated through the corresponding EDX spectrum (Fig.SI.14). The predominant and sharp peaks of Titanium (Ti) at ~ 4.51 keV and Oxygen (O) at ~ 0.52 keV confirm the successful formation of the host TiO_2 matrix. Crucially, the definitive signals corresponding to Silver (Ag) at ~ 3.00 keV and Europium (Eu) lines between 1.1–1.7 keV confirm the successful chemical incorporation of the targeted dopants. The observed deviations between the quantitative EDX data and theoretical compositions are strongly supported by the microstructural findings in Fig. SI.13. Specifically, the slight deficit in the detected Ag content (7.1% vs. theoretical 8.7%) is directly attributed to the localized partial aggregation of metallic nanoparticles explicitly visualized in the high-magnification SEM images (Fig. 1a and b), which locally diminishes the spatial visibility of the element. Similarly, the lower experimental value of Eu (3.5% vs. theoretical 4.3%) corroborates the hypothesis that Eu^{3+} ions are deeply embedded within the internal core lattice of the porous TiO_2 framework rather than residing exclusively on the immediate outer surface, making them less accessible within the effective EDX interaction volume. Conclusively, the combined analysis of the sequential SEM analysis and the EDX spectrum provides robust empirical proof for the successful synthesis of a structurally sound, chemically homogeneous Eu^{3+}-doped Ag-TiO_2 photoanode optimized for high-performance photovoltaic applications.

3.2 Molecular geometries and electronic properties

The optimized molecular structures and some of the geometrical parameters of the molecules are given in Figure SI.1 and Table SI.3. The benzene-imidazole bond length ($r_{1C\text{-}11N}$) and benzene-carbazole ($r_{32C\text{-}2C}$) values are 1.46, and 1.42 A° for L1 compound. The dihedral angle values between carbazole and imidazole ring ($d_{32C\text{-}2C\text{-}1C\text{-}11N}$) is − 152.23° for L1. The calculated dihedral angles for imidazole and carbazole of the L2 structure are 0.29° ($d_{9C\text{-}2C\text{-}3C\text{-}34N}$) and 1.39° ($d_{9C\text{-}2C\text{-}4C\text{-}35N}$). According to the results obtained, the addition of an extra carbazole unit led to a decrease in the dipole moment value of the L2 compound but did not have a significant effect on the bond length values.

DFT is extensively used to interpret important chemical concepts of molecular structure and reactivity [35]. Frontier Molecular Orbitals (FMO) are especially important to comprehend chemical activity of compounds. It also gives insight for the suitability of the materials to be used as DSSC [36]. The calculated results for energies of FMO and global reactivity parameters are listed in (Table 2).

To spontaneously function, dyes must energetically possess an E_{LUMO} higher than the conduction band of TiO_2 (− 4.0 eV) and an E_{HOMO} lower than the I^-/I_3^- electrolyte potential (− 4.8 eV) [37]. Computational results confirm that both investigated compounds satisfy these prerequisites for regeneration as thermodynamically favourable process (Table 2). Since, the calculated energy results cannot be compared directly with the experimental results, the obtained values are only to help determine whether thermodynamic prerequisites,are met or not. The spatial electron density distributions of the frontier molecular orbitals (FMOs) are illustrated in (Fig. 2). For the L1 compound, the HOMO is delocalized throughout the entire molecular framework, whereas the LUMO spans the molecule but excludes the carbazole moiety. Regarding the L2 architecture, (Fig. 2) reveals that the HOMO is selectively localized on the carbazole unit, whereas the LUMO is predominantly accommodated by the π-bridge and the 1,10-phenanthroline group. The electrons are transferred from the carbazole unit to the π-bridge and the 1,10-phenanthroline group within the molecule.

The energy gap between HOMO and LUMO is also crucial for determining the electrical properties of a molecule [35]. As shown in (Table 2), the energy difference (ΔE) is smaller for the L1 compound, indicating that intermolecular electron transfer is more favourable in this compound. Consequently, L1 has a higher DSSC potential. The diminished HOMO–LUMO energy gap of L1 signifies a thermodynamically facilitated electronic excitation alongside highly efficient charge-transfer kinetics. This quantum-chemical insight stands in excellent consonance with the superior PCE metrics manifested experimentally by the L1-based configurations. The results indicate that the axially positioned π-conjugated bridge facilitates efficient charge transfer, which can be strategically exploited to engineer more effective DSSC architectures.

For understanding of the reactive nature of the compounds, global reactivity parameters are evaluated. According to calculations, L1 compound is more reactive. Its hardness and electrophilic index values are 1.89 and 3.23 eV. When, carbazole unit substituted to meta position reactivity of the compound decreases. In addition to this, the reactivity of the compounds increases in methanol medium. The calculated hardness values for L1 and L2 molecules are 1.91 and 1.96 eV, respectively for methanol medium.

The Molecular Electrostatic Potential (MEP) surface is a three-dimensional visualization of the charge distribution. It gives valuable information about the nucleophilic and electrophilic sites of the compounds. An electrostatic potential map consists of red and blue color ranges. Red represents negative potential areas, while blue represents positive potential areas [38, 39]. The MEP surfaces of the compounds are shown in (Fig. 2). As seen in (Fig. 2), the red areas are on the nitrogen atoms of the 1,10-phenanthroline group,

Table 2 Calculated Global Reactivity Descriptors of L1 and L2 Sensitizers in Vacuum and Methanol Media (in *eV*)

		E_{HOMO}	E_{LUMO}	ΔE	η	μ	ω	S
Vacuum	L1	−5.39	−1.60	3.79	1.89	−3.50	3.23	0.26
	L2	−5.53	−1.73	3.80	1.90	−3.63	3.47	0.26
Methanol	L1	−5.45	−1.63	3.82	1.91	−3.54	3.27	0.26
	L2	−5.61	−1.70	3.91	1.96	−3.66	3.42	0.26

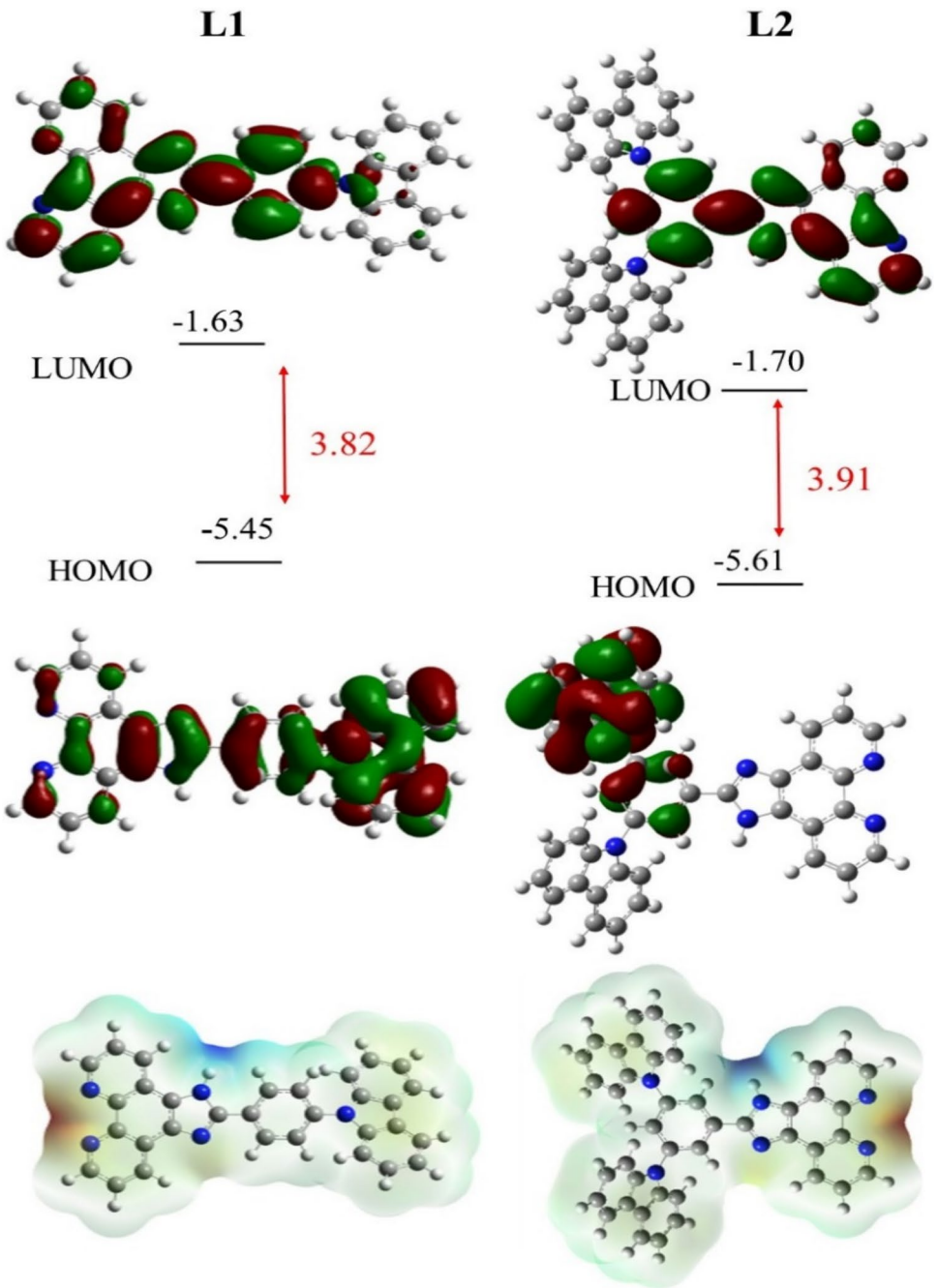


Fig. 2 Energy levels of the frontier molecular orbitals, and MEP of compounds L1 and L2

indicating that they are primary electron-rich regions. Regions with high positive potential are on the carbazole unit and π- bridge.

The light-harvesting efficiency (*LHE*) plays a pivotal role in dictating the short-circuit current density (J_{sc}) of DSSCs, where a higher *LHE* value directly translates into enhanced photocurrent generation. The *LHE* can be theoretically evaluated using the following equation [40, 41]:

$$LHE = 1 - 10^{-f} \quad (5)$$

where *f* denotes the oscillator strength corresponding to the primary electronic transition. Notably, the calculated *LHE* value of L1 (0.83) is substantially higher than that of L2 (0.55), indicating that L1 possesses an inherently superior capacity to capture incident photons. This theoretical trend provides a robust rationale not only for the undoped reference cells but also for

the monumental photocurrent enhancement observed in the co-doped configurations. There may be a relationship between the calculated LHE values and the photovoltaic performances of dyes. In the undoped devices, the superior *LHE* of L1 yields a higher Jsc (0.25 mA/cm^2) compared to TiO_2-L2 (0.23 mA/cm^2). Intriguingly, integrating the photoanode with the ternary Ag–TiO_2–Eu^{3+} architecture may provide additional benefits through the combined effects of Ag-related optical enhancement and the potential optical down-conversion contribution of Eu^{3+} ions. The high light-harvesting capacity of L1 (0.83) provides a favorable basis for investigating these effects. Consequently, the (Ag–TiO_2–Eu)-L1 architecture delivers a prominent escalation in J_{sc}, jumping from 0.25 to 0.39 mA/cm^2 (a 56% improvement). Conversely, due to its severely limited intrinsic *LHE* (0.55), L2 cannot fully exploit the optical localized fields generated by the Ag/Eu dopants, resulting in a more moderate photocurrent increment (rising from 0.23 to 0.32 mA/cm^2). The obtained results are not conclusive because, the calculated LHE depends on solely the primary transition. Furthermore, the calculated LHE values belong only to dye models. They are not valid to dye systems adsorbed on the photoanode. Nevertheless, these findings demonstrate that strategically pairing a high-*LHE* sensitizer with a plasmonic/rare-earth co-doped photoanode may be a suitable approach to increase charge generation in next-generation photovoltaics.

3.3 Photovoltaic performances for DSSC

The comprehensive fabrication procedure of the solar cell devices is detailed in the Device Preparation section. The photocurrent density–voltage (*J–V*) characteristics of the photovoltaic devices fabricated utilizing sensitizers L1 and L2, recorded under simulated solar illumination of 100 mW cm^{-2}, are presented in (Figs. 3 and 4).

The photovoltaic performances of the synthesized L1 and L2 dyes in DSSC applications were evaluated via current–voltage (*J-V*) characteristics and correlated with Density Functional Theory (DFT) calculations. The experimental outcomes revealed that the TiO_2-L1 based cell achieved higher power conversion efficiency (η) of 0.072%, outperforming the TiO_2-L2 based device (0.065%).

The relatively low short-circuit current densities (J_{sc}; 0.25 mA/cm^2 for L1 and 0.23 mA/cm^2) for L2) and overall device efficiencies are inherently tied to the wide HOMO–LUMO energy gaps (*Eg*) of the molecules. As determined by DFT calculations, the wide band gaps of L1 (3.82 eV) and L2 (3.91 eV) restrict their photon harvesting capacity predominantly to the UV region, limiting absorption within the visible solar spectrum. Nevertheless, the narrower energy gap of L1 compared to L2 induces a slight bathochromic shift, extending its excitation profile further towards the visible threshold. This optical advantage translates into

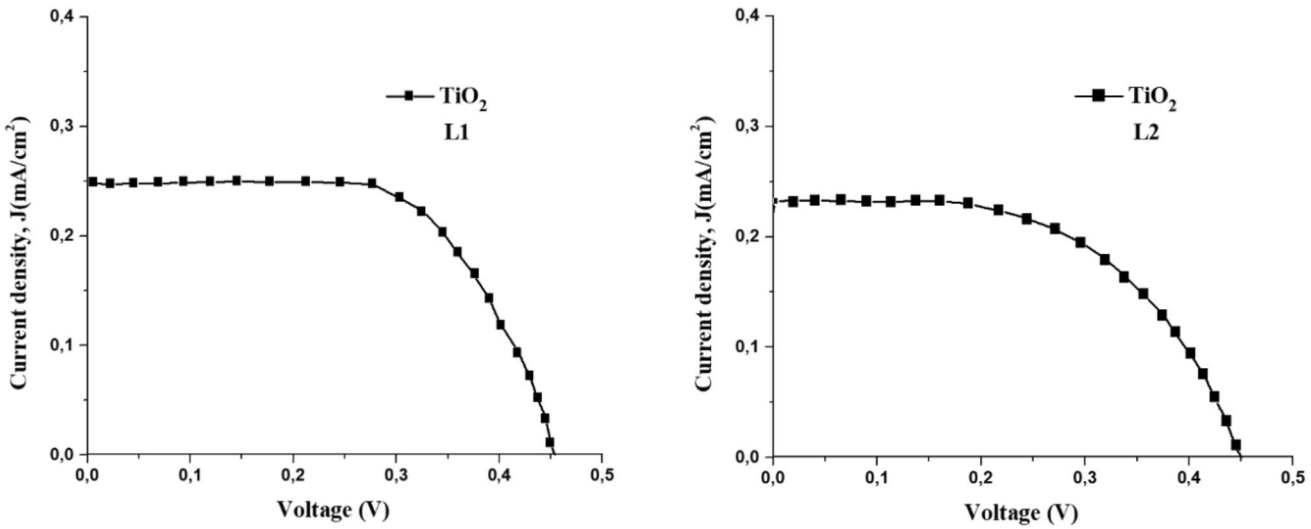


Fig. 3 Current density–voltage (*J–V*) profile of the L1-sensitized reference TiO_2 solar cell under simulated AM 1.5 G solar illumination (100 mW cm^{-2})

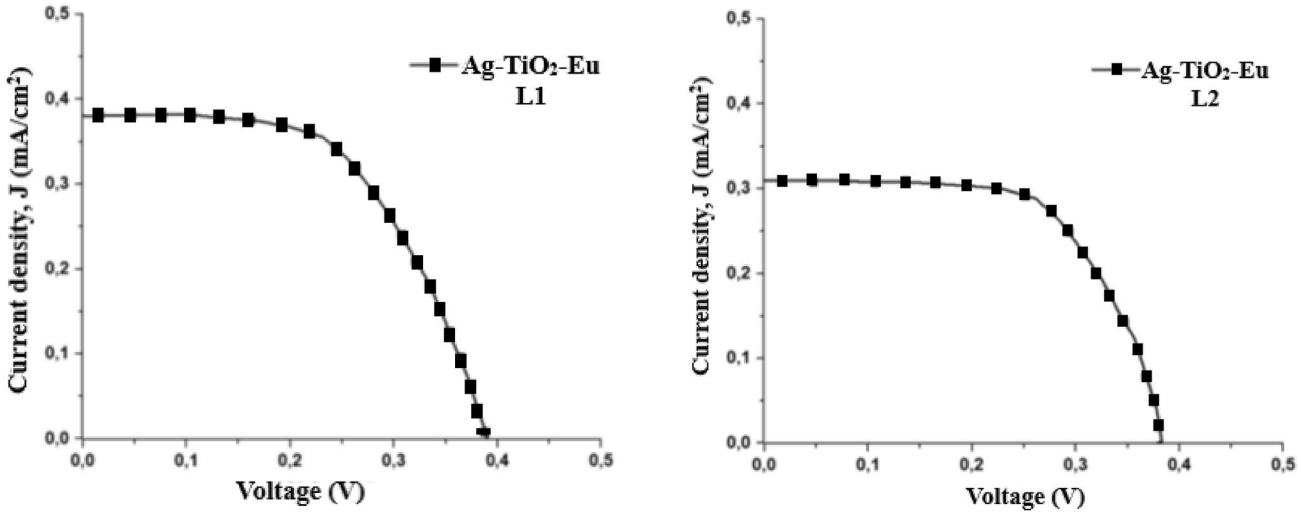


Fig. 4 Current density–voltage (*J–V*) curves of DSSCs based on Eu^{3+}-doped Ag-TiO_2 photoanodes sensitized with L1 and L2 molecules under simulated AM 1.5 G solar illumination (100 mW cm^{-2})

an 8.7% enhancement in (J_{sc}) for L1 by securing a more efficient photon-to-current conversion.

Theoretical frontier molecular orbital analysis indicated that L2 possesses a prominent intramolecular charge transfer (*ICT*) character with well-separated donor–acceptor domains. Although this spatial separation is theoretically expected to suppress charge recombination and boost the open-circuit voltage (V_{oc}), experimental results paradoxically showed a slightly lower voltage for L2 (0.44 V) than L1 (0.45 V). This discrepancy can be attributed to the steric hindrance imposed by the bulky aromatic peripheral rings of L2. As the structure of L2 is different from L1 (Figure SI-1 and Table SI-3), the charge transfer process in the L2 dye may be hindered compared to that in the L1 dye. The large spatial footprint of L2 suppresses the dye loading density on the TiO_2 photoanode surface, leaving exposed semiconductor sites. Consequently, electrons injected into the TiO_2 conduction band undergo back-electron transfer to the triiodide (I^-_3) redox electrolyte via these vacant sites, diminishing the (V_{oc}). Collectively, owing to its dual advantage in both current density and voltage parameters, L1 emerges as a more effective sensitizer for DSSC configurations compared to L2.

The correlation of the morphological (SEM), elemental (EDX), and photovoltaic (*J-V*) findings obtained in this study elucidates a definitive structure–property-performance relationship for the synthesized Ag/TiO_2:Eu^{3+} co-doped nanomaterial as a functional photoanode in DSSCs. High-resolution SEM micrographs confirm that the photoanode matrix comprises highly uniform primary nanoparticles with an average size of ~ 9.59 nm. This nanoscale confinement drastically enhances the specific surface area of the photoanode film, thereby facilitating maximized chemisorption density for both L1 and L2 sensitizer molecules. Simultaneously, the mesoporous agglomeration topography observed in low-magnification SEM views expedites the deep infiltration of the redox electrolyte (I^-/I_3^-) through the film matrix, minimizing mass transport resistance while concurrently functioning as effective light-scattering centres to trap incident photons. The elemental incorporation and chemical purity of the Ag and Eu dopants, validated by EDX spectra, electronically and optically reinforce these morphological advantages.

The photovoltaic performance of the DSSCs was evaluated by comparing the current–voltage (J–V) characteristics and the corresponding photovoltaic parameters, including the open-circuit voltage (Voc), short-circuit current density (Jsc), fill factor (FF), and power conversion efficiency (PCE). Device fabrication and measurement conditions were kept consistent to enable a reliable comparison of L1- and L2-sensitized cells based on undoped TiO_2 and Ag–TiO_2–Eu^{3+} photoanodes. It should be noted that this study focused on a comparative evaluation rather than the comprehensive optimization of parameters such as film thickness, dye adsorption time, and electrolyte concentration.

Table 3 Photovoltaic performance characteristics of L1 and L2-sensitized reference and modified Ag-TiO_2:Eu^{3+} solar cells

Dye	V_{oc}	J_{sc}	Fill Factor	Efficiency
TiO_2-L1	0.45	0.25	0.64	0.072
TiO_2-L2	0.44	0.23	0.64	0.065
(Ag–TiO_2–Eu)-L1	0.39	0.39	0.59	0.090
(Ag–TiO_2–Eu)-L2	0.38	0.32	0.67	0.081

Considering the microstructural characteristics of the modified photoanodes, the photovoltaic results in Table 3 show that the Ag–TiO_2–Eu^{3+}-modified devices exhibit higher power conversion efficiencies than the undoped TiO_2 reference cells. Specifically, the PCE increased from 0.072% for the TiO_2-L1 device to 0.090% for the (Ag–TiO_2–Eu^{3+})-L1 device, corresponding to a relative enhancement of 25% under the investigated conditions. The primary driver behind this enhancement is the substantial improvement in the short-circuit current density (Jsc) from 0.25 to 0.39 mA. cm^{-2}.

The observed decrease in Voc from 0.45 to 0.39 V upon Ag–TiO_2–Eu^{3+} modification can be ascribed to a downward shift in the conduction band edge of TiO_2 induced by electronic interactions with the co-dopants, alongside the potential formation of surface defect states that accelerate charge recombination under open-circuit conditions. Despite this voltage loss, the photoanode modification successfully aligns with the primary objective of improving cell performance; the substantial enhancement in Jsc effectively counterbalances the Voc deficit. Consequently, the combined modification strategy yields improved overall efficiency, validating the viability of this integrated approach.

The modified photoanode may enhance photocurrent through changes in morphology and interfacial charge transport, with a possible contribution from Ag-mediated light harvesting. However, the specific role of surface plasmon resonance (SPR) cannot be confirmed from photovoltaic measurements alone. Similarly, Ag may influence electron transport and charge collection, while Eu^{3+} may modify the defect environment and charge-carrier recombination behavior of TiO_2. Their individual contributions and the underlying charge-transfer mechanisms remain a subject for further investigation, and broader comparisons require consideration of differences in device architecture and experimental conditions.

4 Conclusion

The findings of this study reveal that both theoretical computations and experimental photovoltaic measurements consistently verify the newly designed L1 dye as a more suitable candidate than its L2 analogue for DSSC applications. Furthermore, the obtained PCE values demonstrate the potential of combining D–π–A organic sensitizers featuring a single phenanthroline anchoring unit with Eu^{3+}-modified Ag–TiO_2 photoanodes as a promising approach for improving the photovoltaic performance of dye-sensitized solar cells. The DSSC fabricated with the undoped L1 dye exhibited a baseline PCE of 0.072%. Notably, the incorporation of the modified Eu^{3+}-doped Ag-TiO_2 photoanode elevated the conversion efficiency to 0.090%, corresponding to a substantial 25% enhancement. Ultimately, this study contributes to the literature by introducing novel organic dyes and elucidating the influential effects of modified semiconductor materials on the operational performance of dye-sensitized solar cells (DSSCs). This successful implementation not only bridges the gap between sophisticated molecular engineering and semiconductor modification but also underscores the transformative potential of combining 1,10-phenanthroline-anchored D–π–A architectures with Europium-doped Ag-TiO_2 photoanodes for upscale photovoltaic applications.

Author contributions

I.E. and B.O. designed the experiments. S.A. and A.H. performed all theoretical calculations. I.E. and B.O wrote the main manuscript.

Funding

This work was supported by Yildiz Technical University Scientific Research Project Coordinator's FBA-2023-5930 project.

Data availability

No datasets were generated or analysed during the current study.

Declarations

Conflict of interest The authors declare no competing interests.

Ethical approval Not applicable.

Consent for publication Not applicable.

Human or animal rights Not applicable.

Supplementary Information The online version contains supplementary material available at https://doi.org/10.1007/s10854-026-18850-0.

References

1. B. O'Regan, M. Grätzel, A low-cost, high-efficiency solar cell based on dye-sensitized colloidal TiO2 films. Nature **353**, 737–740 (1991). https://doi.org/10.1038/353737a0
2. M. Grätzel, Dye-sensitized solar cells. J. Photochem. Photobiol. C, Photochem. Rev. **4**, 145–153 (2003). https://doi.org/10.1016/S1389-5567(03)00026-1
3. J.V.S. Krishna, M. Mrinalini, S. Prasanthkumar, L. Giribabu, *Dye-Sensitized Solar Cells* (Elsevier, 2019), pp.231–263
4. M. Hosseinnezhad, S. Nasiri, V. Nutalapati, K. Gharanjig, A.M. Arabi, A review of the application of organic dyes based on naphthalimide in optical and electrical devices. Prog. Color Colorants Coat. **17**(4), 417–433 (2024). https://doi.org/10.30509/pccc.2024.167247.1267
5. S. Dodia, G. Jadav, T. Dudharejiya, D. Katariya, R. Khunt, B. Kataria, J.H. Markna, Photo-switch: a TD-DFT investigation. Comput. Theor. Chem. **1264**, 115934 (2026). https://doi.org/10.1016/j.comptc.2026.115934
6. a) N. Koumura, Z.-S.Wang, S.Mori, M.Miyashita, E. Suzuki, K. Hara, J. Am. Chem. Soc. 2006, 128, 14256. b) Z. S. Wang, N. Koumura, Y. Cui, M. Takahashi, H. Sekiguchi, A. Mori, T. Kubo, A. Furube, K. Hara, Chem. Mater. 2008, 20, 3993. c) C.-H. Yang, S.-H. Liao, Y.-K. Sun, Y.-Y. Chuang, T.-L. Wang, Y.-T. Shieh,W.-C. Lin, J. Phys. Chem. C 2010, 114, 21786. d) P. Shen, Y. Tang, S. Jiang, H. Chen, X. Zheng, X. Wang, B. Zhao, S. Tan, Org. Electronics 2011, 12, 125.
7. P.K. Rathod, T.K. Pathak, P. Kher, G. Jadav, S. Dodia, K. Khatsuriya, P. Lakhani, D.K. Dhruv, B. Kataria, J.H. Markna, Quasi-intrinsic absorber engineering for electric-field-driven carrier collection in $CdIn_2Se_4$ solar cells. Next Energy **13**, 100752 (2026). https://doi.org/10.1016/j.nxener.2026.100752
8. L. Zhang, J.M. Cole, Anchoring groups for dye-sensitized solar cells. ACS Appl. Mater. Interfaces **7**, 3427–3455 (2015). https://doi.org/10.1021/am507334m
9. T. Higashino, S. Nimura, K. Sugiura, Y. Kurumisawa, Y. Tsuji, H. Imahori, Photovoltaic properties and long-term durability of porphyrin-sensitized solar cells with silicon-based anchoring groups. ACS Omega **2**, 6958–6967 (2017). https://doi.org/10.1021/acsomega.7b01290
10. N.H. Vaosya, R. Zala, G. Jadav, D.K. Katariya, R. Khunt, B. Kataria, J.H. Markna, Computational insights into alizarin for toy applications using DFT calculations of photophysical properties and spectroscopic safety. Discover Chemistry **3**, 482 (2026). https://doi.org/10.1007/s44371-026-00939-4
11. P. Naik, M.R. Elmorsy, R. Su, D.D. Babu, A. El-Shafei, A.V. Adhikari, New carbazole based metal-free organic dyes with D–π–A–π–A architecture for DSSCs: synthesis, theoretical and cell performance studies. Sol. Energy **153**, 600–610 (2017). https://doi.org/10.1016/j.solener.2017.05.088
12. P. Naik, I.M. Abdellah, M. Abdel-Shakour, K.S. Keremane, A.V. Adhikari, Enhancing the photoelectrochemical performance of Ru(II)-sensitized dye-sensitized solar cells using cyanopyridine-based cosensitizers. Energy Technol. **13**, 2500294 (2025). https://doi.org/10.1002/ente.202500294
13. K.S. Keremane, I.M. Abdellah, M.R. Eletmany, P. Naik, P. Anees, A.V. Adhikari, Push–pull carbazole twin dyads as efficient sensitizers/co-sensitizers for DSSC application: effect of various anchoring groups on photovoltaic performance. J. Mater. Chem. C **13**, 9258 (2025). https://doi.org/10.1039/D4TC04612A
14. L.P. Zhang, K.J. Jiang, Q. Chen, G. Li, L.-M. Yang, Pyrazino-[2,3-f][1,10]phenanthroline as a new anchoring group of organic dyes for dye-sensitized solar cells. RSC Adv. **5**, 46206–46209 (2015). https://doi.org/10.1039/C5RA05349H
15. H.L. Jia, Z.J. Peng, B.-Q. Gong, C.-Y. Huang, M.-Y. Guan, New 2D–π–2A organic dyes with bipyridine anchoring groups for DSSCs. New J. Chem. **43**, 5820–5825 (2019). https://doi.org/10.1039/C9NJ00087A
16. B. Ozsan, S. Aydogdu, A. Hatipoglu, I. Erden, Synthesis, theoretical and photovoltaic investigation of two 1,10-phenanthroline-based D–π–A organic dyes for dye-sensitized solar cells. Chem. Pap. (2026). https://doi.org/10.1007/s11696-026-04746-0
17. Y.X. Dong, X.L. Wang, E.M. Jin, S.M. Jeong, B. Jin, S.H. Lee, One-step hyrothermal synthesis of Ag decorated TiO2 nanoparticles for dye-sensitized solar cell application.

Renew. Energy **135**, 1207–1212 (2019). https://doi.org/10.1016/j.renene.2018.12.062

18. E. Akman, S. Akin, T. Ozturk, B. Gulveren, S. Sonmezoglu, Europium and terbium lanthanide ions co-doping in TiO_2 photoanode to synchronously improve light-harvesting and open-circuit voltage for high-efficiency dye-sensitized solar cells. Sol. Energy **202**, 227–237 (2020). https://doi.org/10.1016/j.solener.2020.03.108
19. V. Kumar, S.K. Swami, A. Kumar, O.M. Ntwaeaborwa, V. Dutta, H.C. Swart, Eu^{3+} doped down shifting TiO2 layer for efficient dye-sensitized solar cells. J. Colloid Interface Sci. **484**, 24–32 (2016). https://doi.org/10.1016/j.jcis.2016.08.060
20. M. Grätzel, Conversion of sunlight to electric power by nanocrystalline dye-sensitized solar cells. J. Photochem. Photobiol. A: Chem. **164**, 3–14 (2004). https://doi.org/10.1016/j.jphotochem.2004.08.014
21. G.P. Smestad, Education and solar conversion: demonstrating electron transfer. Sol. Energy Mater. Sol. Cells **55**, 157–178 (1998). https://doi.org/10.1016/S0927-0248(98)00056-7
22. G.F. Smith, W. Cagle, The Improved Synthesıs Of 5-Nıtro-1, 10-Phenanthrolıne. J. Org. Chem. **12**, 781–784 (1947). https://doi.org/10.1021/jo01170a007
23. J. Bolger, A. Gourdon, E. Ishow, J.-P. Launay, Mononuclear and binuclear tetrapyrido[3,2-*a*:2′,3′-*c*:3″,2″-*h*:2‴,3‴-*j*] phenazine (tpphz) ruthenium and osmium complexes. Inorg. Chem. **35**(10), 2937–2944 (1996). https://doi.org/10.1021/ic951436w
24. Z. Si, X. Li, X. Li, G. Xu, C. Pan, Z. Guo, H. Zhang, L. Zhou, Novel Re(I) dendrimers: synthesis, characterization and theoretical studies. Dalton Trans. **47**, 10592–10600 (2009). https://doi.org/10.1039/b912939a
25. M. J. Frisch, G. W. Trucks, H. B. Schlegel, G. E. Scuseria, M. A. Robb, J. R. Cheeseman, J. A. Montgomery, T. Vreven, K. N. Kudin, J. C. Burant, J. M. Millam, S. S. Iyengar, J. Tomasi, V. Barone, B. Mennucci, M. Cossi, G. Scalmani, N. Rega, G. A. Petersson, H. Nakatsuji, M. Hada, M. Ehara, K. Toyota, R. Fukuda, J. Hasegawa, M. Ishida, T. Nakajima, Y. Honda, O. Kitao, H. Nakai, M. Klene, X. Li, J. E. Knox, H. P. Hratchian, J. B. Cross, C. Adamo, J. Jaramillo, R. Gomperts, R. E. Stratmann, O. Yazyev, A. J. Austin, R. Cammi, C. Pomelli, J. W. Ochterski, P. Y. Ayala, K. Morokuma, G. A. Voth, P. Salvador, J. J. Dannenberg, V. G. Zakrzewski, S. Dapprich, A. D. Daniels, M. C. Strain, O. Farkas, D. K. Malick, A. D. Rabuck, K. Raghavachari, J. B. Foresman, J. V. Ortiz, Q. Cui, A. G. Baboul, S. Clifford, J. Cioslowski, B. B. Stefanov, G. Liu, A. Liashenko, I. Piskorz, I. Komaromi, R. L. Martin, D. J. Fox, T. Keith, M. A. Al-Laham, C. Y. Peng, A. Nanayakkara, P. M. W. Challacombe, P. W. Gill, B. Johnson, W. Chen, M. W. Wong, C. Gonzalez, J. A. Pople, Gaussian 09, Revision C.01, Gaussian, Inc., Pittsburgh, PA, 2009.
26. M. Cossi, N. Rega, G. Scalmani, V. Barone, Energies, structures, and electronic properties of molecules in solution with the C-PCM solvation model. J. Comput. Chem. **24**, 669–681 (2003). https://doi.org/10.1002/jcc.10189
27. V. Barone, M. Cossi, J. Tomasi, J. Comput. Chem. **19**, 404–417 (1998)
28. B.N. Sundaraganesan, S. Ilakiamani, H. Saleem, P.M. Wojciechowski, D. Michalska, 2005, FT-Raman and FT-IR spectra, vibrational assignments and density functional studies of 5-bromo-2-nitropyridine. SpectrochimicaActa **61**(13–14), 2995–3001 (2005). https://doi.org/10.1016/j.saa.2004.11.016
29. K. Wolinski et al., Efficient implementation of the gauge-independent atomic orbital method for NMR chemical shift calculations. J. Am. Chem. Soc. **112**, 8251–8260 (1990). https://doi.org/10.1021/ja00179a005
30. R.G. Pearson, Absolute Electronegativity and Hardness: Applications to. Org. Chem. (1989). https://doi.org/10.1021/jo00267a034
31. R.G. Parr et al., Electrophilicity Index (1999). https://doi.org/10.1021/ja983494x
32. P. Geerlings et al., Concept. Density Funct. Theory. (2003). https://doi.org/10.1021/cr990029p
33. R. Dennington, T. Keith, J. Millam, *GaussView, Version 5* (Semichem Inc., Shawnee Mission, KS, 2009)
34. S. Aydogdu, A. Hatipoglu, Theoretical insight into the degradation reaction of cefradine in aqueous medium: mechanism, kinetics, and ecotoxicity. J. Indian Chem. Soc. **102**, 102164 (2025). https://doi.org/10.1016/j.jics.2025.102164
35. S. Aydoğdu, A. Hatipoğlu, A. Erdoğmuş, J. Comput. Biophys. Chem. **21**, 599–609 (2022). https://doi.org/10.1142/s2737416522500235
36. S. Aydogdu, A. Hatipoglu, The reaction mechanism investigation of sulfonamides with OH radical by DFT. J. Indian Chem. Soc. **99**, 100752 (2022). https://doi.org/10.1016/j.jics.2022.100752
37. A. Abdelaaziz et al., Enhancing the performance of triazatruxene-based D-π-A organic dyes containing different π-spacer for dye-sensitized solar cells applications: DFT/TD-DFT study. Dyes Pigments **247**, 113437 (2026). https://doi.org/10.1016/j.dyepig.2025.113437
38. S. Aydogdu, A. Hatipoglu, Electronic structures and reactivities of COVID-19 drugs: a DFT study. Acta Chim. Slov. **69**, 647–656 (2022). https://doi.org/10.17344/acsi.2022.7522

39. I. Erden, A. Hatipoğlu, C. Cebeci, S. Aydoğdu, J. Mol. Struct. **1201**, 127202 (2020). https://doi.org/10.1016/j.molstruc.2019.127202
40. M. Ishtiaq et al., Structural modification of A-C-A configured X–PCIC acceptor molecule for efficient photovoltaic properties with low energy loss in organic solar cells. J. Mol. Graph. Model. **129**, 108722 (2024). https://doi.org/10.1016/j.jmgm.2024.108722
41. Al-Fatlawe et al., Design and analysis of novel D–π–A configuration dyes for dye-sensitized solar cells: a density functional theory study. J. Comput. Electronics **24**(2), 62 (2025). https://doi.org/10.1007/s10825-025-02303-8

Publisher's Note Springer Nature remains neutral with regard to jurisdictional claims in published maps and institutional affiliations.

Springer Nature or its licensor (e.g. a society or other partner) holds exclusive rights to this article under a publishing agreement with the author(s) or other rightsholder(s); author self-archiving of the accepted manuscript version of this article is solely governed by the terms of such publishing agreement and applicable law.